International Journal of Microwave and Wireless Technologies

cambridge.org/mrf

Design and optimization of MIMO dielectric resonator antenna with high gain and circular polarization features using machine learning algorithms

Swati Anand Dwivedi[1], Raghavendra Sharma[1] and Vivek Singh Kushwah[2]

[1]Department of Electronics & Communication Engineering, Amity School of Engineering & Technology, Amity University, Gwalior, MP, India and [2]Department of Electronics & Communication Engineering, Chaitanya Bharathi Institute of Technology, Hyderabad, TS, India

Research Paper

Cite this article: Dwivedi SA, Sharma R, Kushwah VS (2025) Design and optimization of MIMO dielectric resonator antenna with high gain and circular polarization features using machine learning algorithms. *International Journal of Microwave and Wireless Technologies* **17**(3), 504–513. https://doi.org/10.1017/S1759078725101694

Received: 18 September 2024
Revised: 12 May 2025
Accepted: 12 May 2025

Keywords:
circular polarization; dielectric resonator antenna; diversity gain; ECC; high directivity; high gain; isolation; machine learning; metasurface; MIMO Antenna

Corresponding author: Vivek Singh Kushwah;
Email: drviveksinghkushwah@gmail.com

Abstract

This paper elaborates the design and analysis of cross-aperture-coupled twin port ceramic radiator. Stimulation of alumina ceramic using a cross slot helps to produce circular waves within 7.35–7.8 GHz. The polarization diversity concept helps to improve the separation level by above 25 dB. Loading of double negative unit cell made metasurface (MS) improves the antenna gain over 11.5 dBi within the working spectrum. Machine learning (ML) techniques, i.e. Decision Tree and Random Forest are utilized to predict the $|S_{11}|$/Axial ratio parameters. Experimental verification/ML prediction and optimized simulated consequences confirm that the structured radiator works efficiently between 7.21 and 8.2 GHz with over 25 dB isolation between the ports. Directive pattern and decent values of (MIMO) parameters make the radiator applicable for the 6G communication system.

Introduction

The efficiency of radio communication in the modern day depends on aerial design. Increased data rate, gain value, and alignment independence may all be obtained with an effective antenna design. A multi-port aerial with circular polarization features can meet these requirements to a great extent. Using diversity technique, multiport aerial may deliver higher data rates without rising signal power [1]. The addition of a circular polarization feature may make a transmitter/receiver antenna orientation independent and reduce the fading impact [2]. To enhance the gain, currently, researchers are using ceramic radiators in place of printed radiator due to their inherent ability to no metallic losses [3]. An aerial parameter refinement is being done using a new idea called machine learning. Many aerial parameter data may be quickly examined via machine learning (ML) approaches [4].

Certain research publications about circularly polarized ceramic-based multiport aerials are published in the public domain literature. Two-port dielectric resonator (DR)-based Multi-Input Multi-Output (MIMO) that is triggered by a perturbed circular aperture was invented by Das et al. With the aid of the polarization diversity idea, it operates in the 5.35–5.8 GHz range and achieves isolation levels exceeding 25 dB [5]. A twin port ceramic circular polarization (CP) radiator designed by Varshney et al. operates between 5.71 and 8.2 GHz and has a 3 dB absorbance ratio between 7.72 and 8.04 GHz [6]. A two-port rectangle DR-based multiport antenna operating in the 2.36–2.59 GHz range was created by Hu et al. Additionally; it supports CP waves within the 2.39–2.51 GHz working range [7]. A polarization translator was created by Reddy et al. and installed above a twin port aerial that was based on DRs. It is compatible with the 5.3–5.51 GHz narrow CP bandwidth [8]. In a similar way, Abhay et al. structured twin port alumina-based radiator, which operates from 5.25 to 6.17 GHz. With assistance of polarization convertor, it supports CP waves from 5.51 to 6.01 GHz [9]. In case of printed antennas, metasurfaces are utilized to enhance the gain as well as to improve the circular polarization bandwidth [10–18].

A number of the research publications on aerial interpreting using ML techniques in microwave spectrum can be found. The many ML techniques being used for antenna tuning and performance prediction are intriguing to see. Zheng et al. used a ML tactic to improve a patch aerial with an emphasis on the estimation of $|S_{11}|$ [19]. Sharma et al. use lasso ML, k-nearest neighbour (KNN), and artificial neural network (ANN) for estimating how a T-shaped patch

© The Author(s), 2025. Published by Cambridge University Press in association with The European Microwave Association.

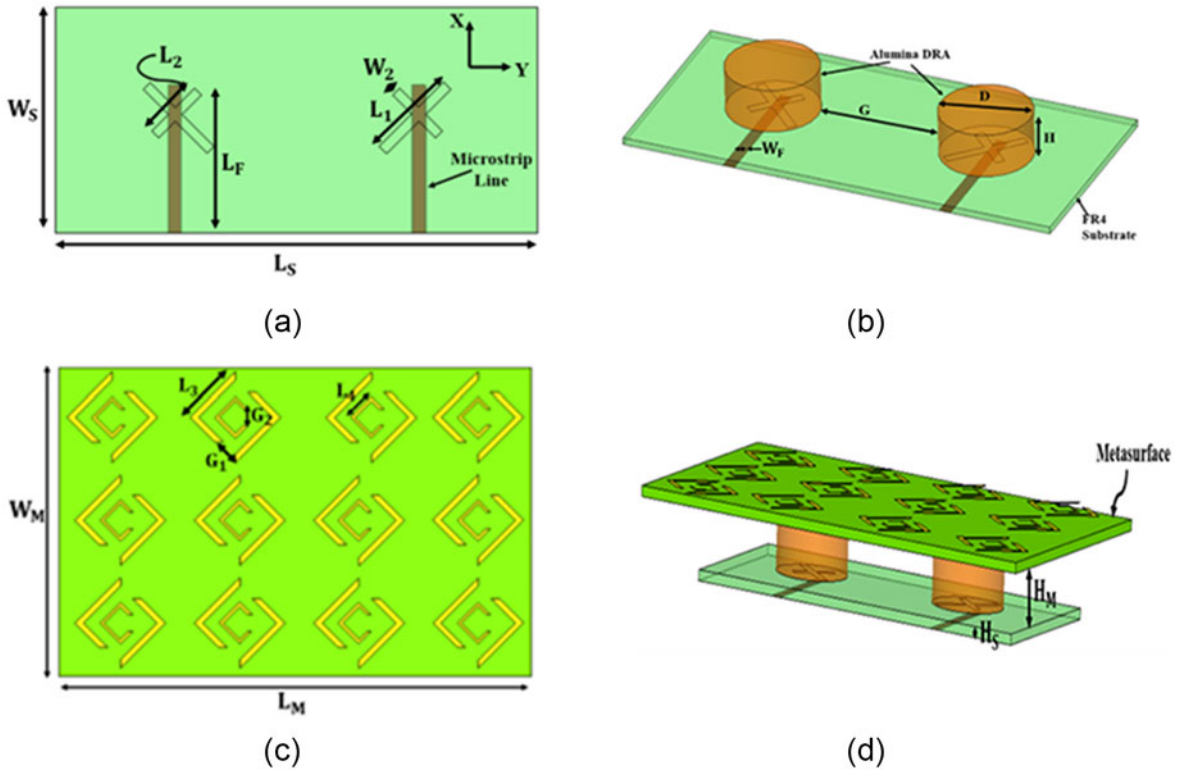


Figure 1. Layout of designed radiator: (a) feed design, (b) ceramic radiator, (c) metasurface design, and (d) 3D view.

Table 1. Optimal sizes of various parameters of designed aerial

Symbol	Size (mm)	Symbol	Size (mm)
L_S	90.0	H_S	1.6
W_S	48.0	L_M	115.0
L_F	29.5	W_M	75.0
W_F	5.0	L_1	14.0
H_M	10.0	L_2	10.0
W_2	2.0	G	10.0
D	15.0	H	7.5
L_3	11.0	L_4	5.0
G_1	5.0	G_2	2.5

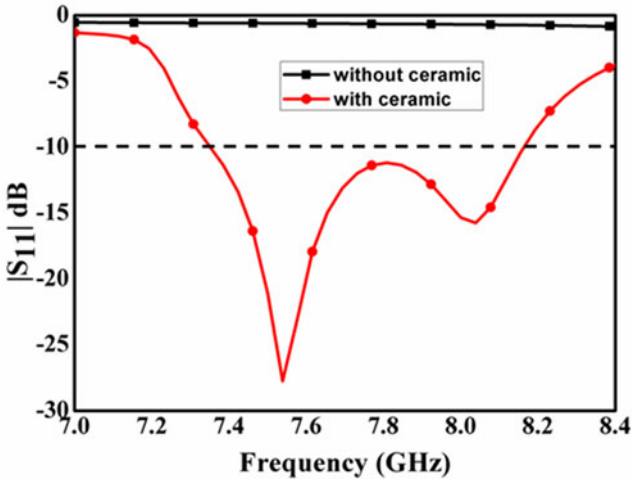


Figure 2. $|S_{11}|$ alteration for one-port radiator with and without ceramic.

would perform. The performance of these ML algorithms was also evaluated by the writers [20]. Various ML techniques are used by Ranjan et al. to improve an ultra-wideband (UWB) printed radiator [21]. In order to forecast the |S11| of a ceramic antenna, Srivastava et al. eliminate disadvantage of ANN with the aid of KBNN [22]. An L-formed stimulated ring dielectric multiport aerial was planned by Pandey et al. It receives circular waves in between 2.8 and 3.05 GHz. Several ML methods are applied to enhance the planned radiator [23].

This communication provides the detailed investigation of twin port dielectric-based aerial loaded with a metasurface (MS). The uniqueness of this antenna design is to get CP, high isolation (more than 25 dB), and high gain (11.5 dBi) simultaneously without effecting the impedance bandwidth of antenna. Addition of ML-based prediction helps to reduce the computational time required by simulator. However, due to the use of MS, overall size of antenna becomes more. This problem can be overcome by using some other technique of gain enhancement like surface integrated waveguide (SIW). To better understand the concept, this paper is segmented in different sections: (i) structural layout of antenna; (ii) antenna analysis; (iii) prediction of S-parameter using ML algorithms; (iv) experimental authentication; and (v) inference.

Structural layout of antenna

Different views/components of designed two-port aerial are shown in Fig. 1 and the sizes of various parameters of designed aerial is listed in Table 1. Alumina-based ceramic ($\varepsilon_r = 9.8$) is used as

https://doi.org/10.1017/S1759078725101694 Published online by Cambridge University Press

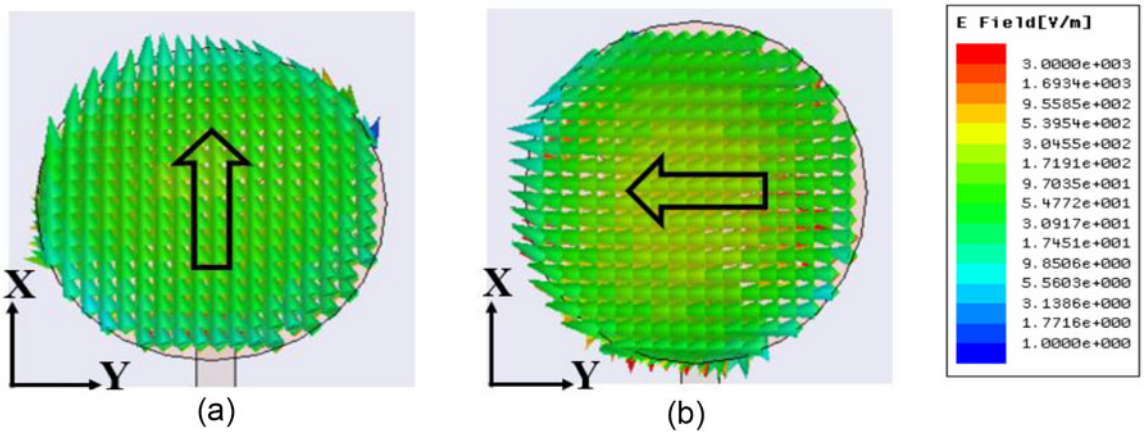


Figure 3. E-field rotation on alumina ceramic (a) 7.58 Ghz (b) 8.1 Ghz.

radiator and placed on the FR4 substrate ($\varepsilon_r = 4.4$). The thickness of substrate is 1.6 mm. Cross-formed slot has been etched from the substrate and created as a feed for ceramic. Printed line is placed in the lower part of substrate and used to feed the cross slot. Metasurface is based on single-sided FR4 substrate with a thickness of 1.6 mm.

Antenna analysis

This segment provides a detailed investigation on proposed two-port ceramic aerial with the assistance of HFSS software. Analysis has been started with one-port radiator. Figure 2 presents the $|S_{11}|$ alteration for single-port aerial with and without alumina ceramic. One significant reflection found from Fig. 2 that the complete working spectrum is because of alumina ceramic. In the working spectrum, two resonances are visible at 7.58 GHz and 8.1 GHz. Vectored E-field lines are plotted in Fig. 3 at 7.58 GHz and 8.1 GHz. It can be perceived from Fig. 3 that dual orthogonal hybrid mode i.e. $HEM^{x}_{11\delta}$ and $HEM^{y}_{11\delta}$ at 7.58 GHz and 8.1 GHz correspondingly [24]. Numerically, the resonance frequency of fundamental hybrid mode is given as follows [25]:

$$f_{r,HEM_{11\delta}} = \frac{6.321c}{\pi D\sqrt{\varepsilon_r + 2}}\left[0.27 + 0.36\left(\frac{D}{4H}\right) + 0.02\left(\frac{D}{4H}\right)^2\right] \quad (1)$$

In eqn. (1), "*c*," "*D*," and "*H*" denote speed of light, diameter, and height of dielectric rod, respectively. From above equation, the resonant frequency is found to be 7.85 GHz, which is closer to resonance obtained in HFSS software.

For finding out the reason of taking cross slot with unequal arm length, Fig. 4(a) and Fig. 4(b) plot the $|S_{11}|$ and axial ratio alteration with three different cases: (i) rectangular slot linked ceramic; (b) X-slot with identical arm size-linked ceramic; and (iii) X-slot with uneven arm size-linked ceramic. Two significant remarks found from Fig. 4: (a) in case three, two resonant peaks occurred, which is due to orthogonal mode; and (b) X-slot with uneven arm size supports CP waves from 7.42 to 7.8 GHz. A variation in the size of one arm of the X-aperture produces a 90° phase difference between the orthogonal modes, and the cross slot aids in the production of twin orthogonal modes within the DRA. Thus, the suggested aperture provides a dual orthogonal mode inside the ceramic with 90° phase changes, which is a prerequisite for the formation of circular polarization [26]. Figure 5 presents the axial ratio alteration with change in dimension L_1. It can be seen from Fig. 5 that the optimized AR bandwidth is obtained when $L_1 = 14.0$ mm.

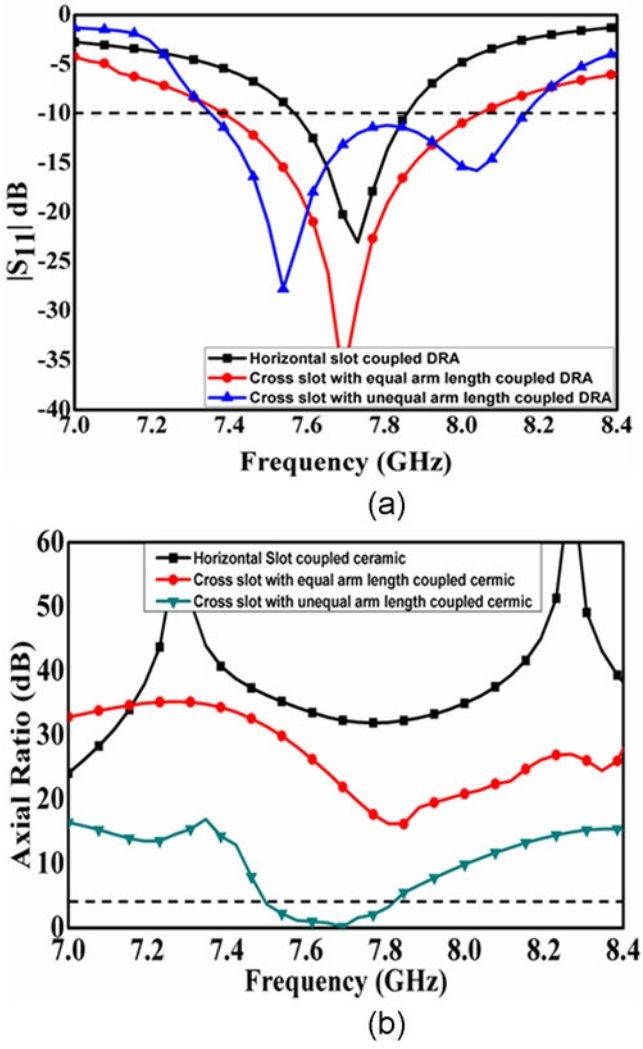


Figure 4. (a) $|S_{11}|$ variation with various alteration in shape of slots and (b) axial ratio variation with various alteration in shape of slots.

https://doi.org/10.1017/S1759078725101694 Published online by Cambridge University Press

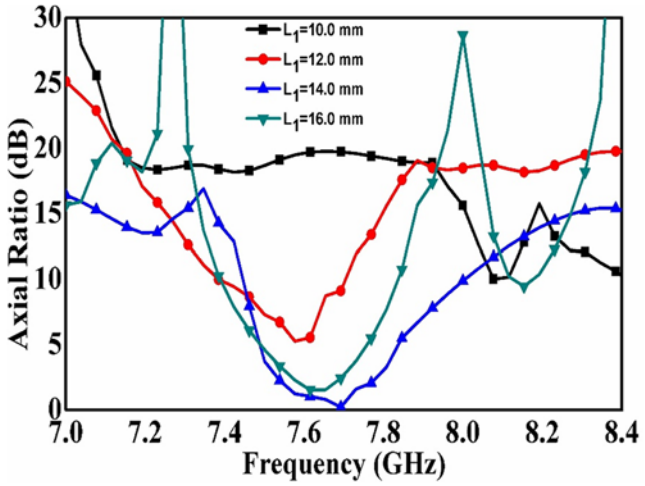


Figure 5. Axial ratio variation with different change in L_1.

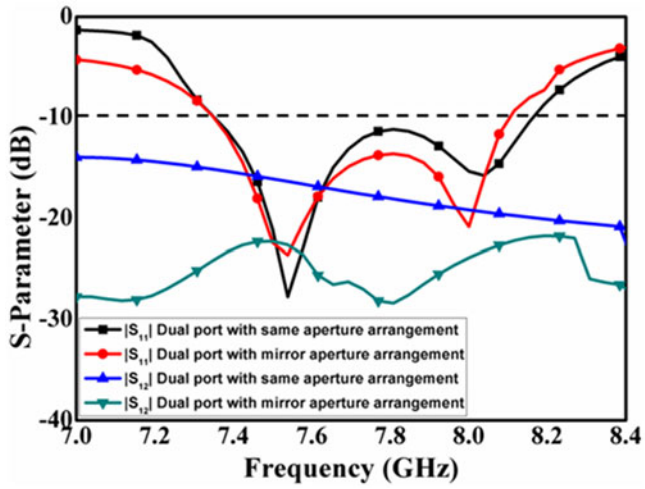


Figure 6. S-parameter alteration for two-port radiator with change in aperture placement.

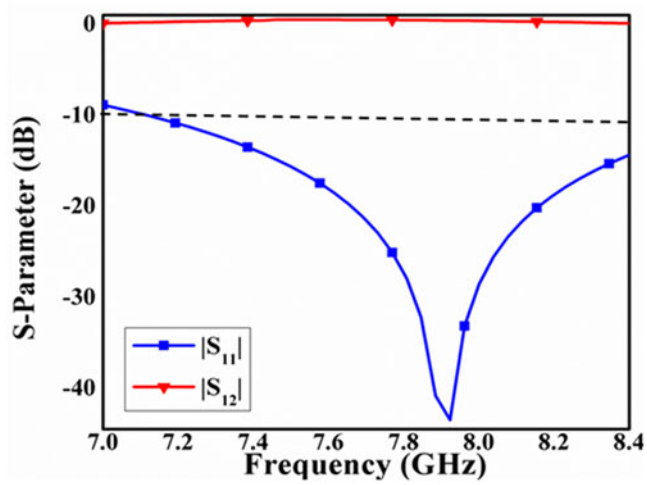


Figure 7. $|S_{11}|/|S_{12}|$ alteration of designed unit cell.

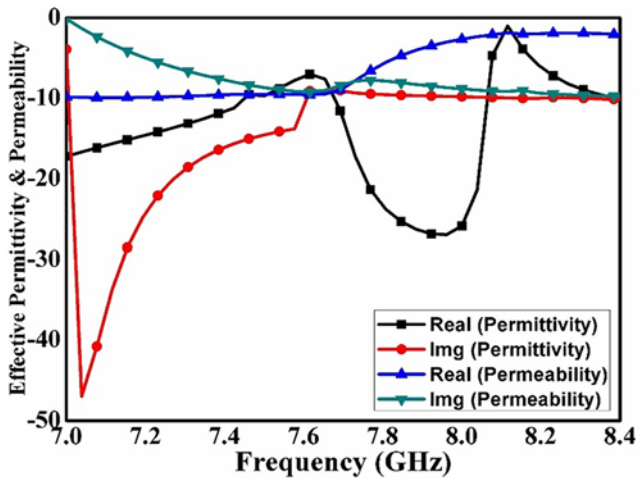


Figure 8. Effective permittivity and permeability of designed unit cell.

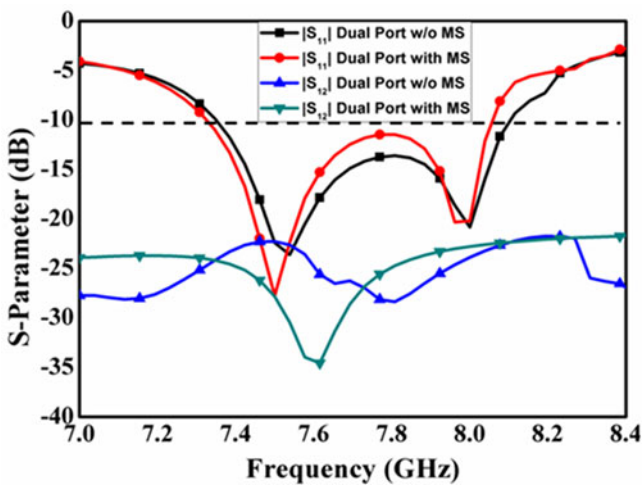


Figure 9. $|S_{11}|/|S_{12}|$ variation of dual port aerial with and without MS.

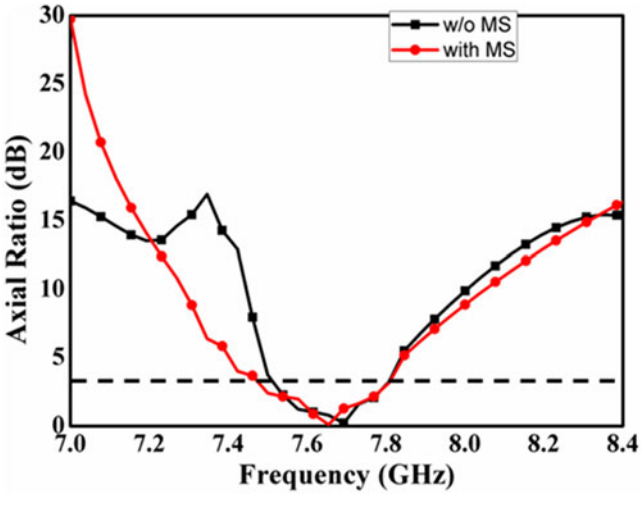


Figure 10. Axial ratio variation of dual port aerial with and without MS.

Single port aerial is converted in dual port with parallel placing of antenna ports. However, the aperture orientation is taken as two ways: (i) same slot placement; and (ii) mirror slot placement. Figure 6 shows the alteration of S-parameter with aforementioned

https://doi.org/10.1017/S1759078725101694 Published online by Cambridge University Press

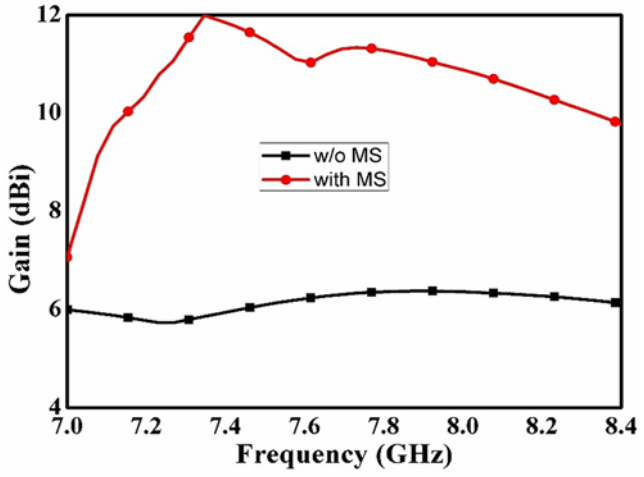


Figure 11. Broadsided gain variation of dual port aerial with and without MS.

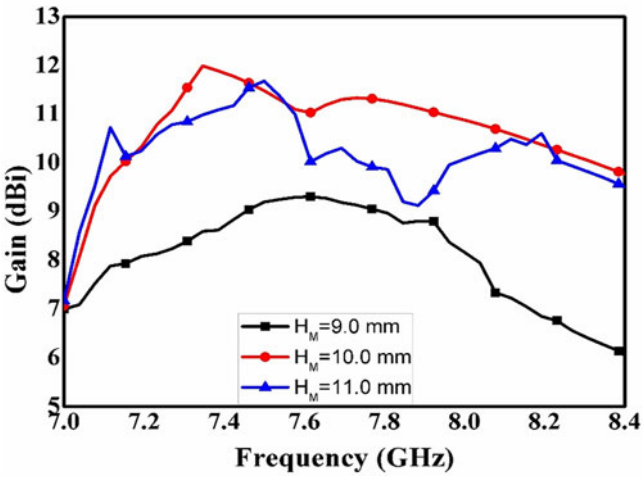


Figure 12. Gain variation with change in H_M.

Table 2. Comparing every model using S11 performance metrics

Algorithm	R^2 Score	MSE	MAE
Decision Tree	0.965	0.756	0.351
Random Forest	0.972	0.687	0.304

Table 3. Comparing every model using axial ratio performance metrics

Algorithm	R^2 Score	MSE	MAE
Decision Tree	0.942	0.824	0.354
Random Forest	0.951	0.752	0.312

two cases. It can be seen from Fig. 6 that $|S_{11}|$ parameter is approx. same in both cases, while the mutual coupling is reduced to less than −25 dB within the working spectrum in case of mirror slot placement. This is because of the polarization diversity concept [5]. Polarization diversity means that the one port supports left-handed CP (LHCP) wave, while other port supports right-handed CP (RHCP).

A MS is suspended over the two-port ceramic radiator. This metasurface is made up of periodic arrangement of unit cell. Figure 7 shows the $|S_{11}|/|S_{12}|$ variation for unit cell. It can be seen from Fig. 7 that $|S_{11}|$ is well below to −10 dB, while $|S_{12}|$ is near to 0 dB with in the working spectrum. This confirms that the unit cell allows the EM waves passes through it. In order to extract the effective dielectric constant and permeability of unit cell, the following equations are utilized [27]:

$$Z = \pm\left[\frac{(1+S_{11})^2 - S_{21}^2}{(1-S_{11})^2 - S_{21}^2}\right]^{0.5} \tag{2}$$

$$e^{j\eta k_0 d} = \frac{S_{21}}{1 - S_{11}\frac{Z-1}{Z+1}} \tag{3}$$

$$\varepsilon = \frac{\eta}{Z} \tag{4}$$

$$\mu = \eta * Z \tag{5}$$

In the above equations, "Z," "d," "k_0," and "η" indicate the input impedance, width of substrate, wave number, and intrinsic impedance, respectively. "S_{11}" and "S_{12}" denote reflection coefficient and mutual coupling, respectively. "ε" and "μ" denotes effective permittivity and permeability, respectively. With the assistance of above equations, effective permittivity and permeability is plotted within the working spectrum and shown in Fig. 8. It can be perceived from Fig. 8 that both permeability and permittivity is negative within the working spectrum. This means that unit cell behaves as double negative material.

Figure 9 presents the S-parameter alteration with and without suspension of MS over the two-port aerial. It can be detected from Fig. 9 that $|S_{11}|$ is approximately same in both circumstances. The mutual coupling level is also same with and without MS. Figure 10 shows the axial ratio variation with and without MS. It is observed from Fig. 10 that the axial ratio curve is also not much effected by placing MS. Broadsided gain variation is shown in Fig. 11 with and without MS. It can be seen from Fig. 11 that the broadsided gain is enhanced to more than 11 dBi after placing MS. Double negative unit cell's made MS improves the directivity, which in turn improves the antenna's gain [28].

Figure 12 shows the gain variation with different changes in the gap between antenna and MS. It can be seen from Fig. 12 that the optimized gain is obtained at 10.0 mm.

Prediction of s-parameter using ML algorithms

Two different ML methods are applied in this section to predict the planned radiator's axial ratio and reflection coefficient (S11). Decision Tree and Random Forest (RF), are the ML methods that have been used for that purpose [21]. A RF voting mechanism selects the main tree as the ultimate output after several trees vote for the outcomes. In ML, decision trees are frequently used to generate and predict results using input data. The architecture resembles a tree, with every inner node testing a property, every branch representing a feature value, and each leaf node representing the ultimate choice or forecast. The main advantage of these two algorithms is to get better accuracy even for smaller data set. After training process, these algorithms are utilized to predict the reflection coefficient and axial ratio value of proposed antenna by simply provides the sizes of various antenna parameters [29, 30]. Collections of data are generated by changing D (13.0–17.0 mm in 0.25 incremental step), H (5.0–10.0 mm in 0.25 incremental step), L_1 (12.0–16.0 mm in 0.25 incremental step), L_2 (8.0–12.0 mm in 0.25 incremental step), H_M (8.0–12.0 mm in 0.25 incremental

https://doi.org/10.1017/S1759078725101694 Published online by Cambridge University Press

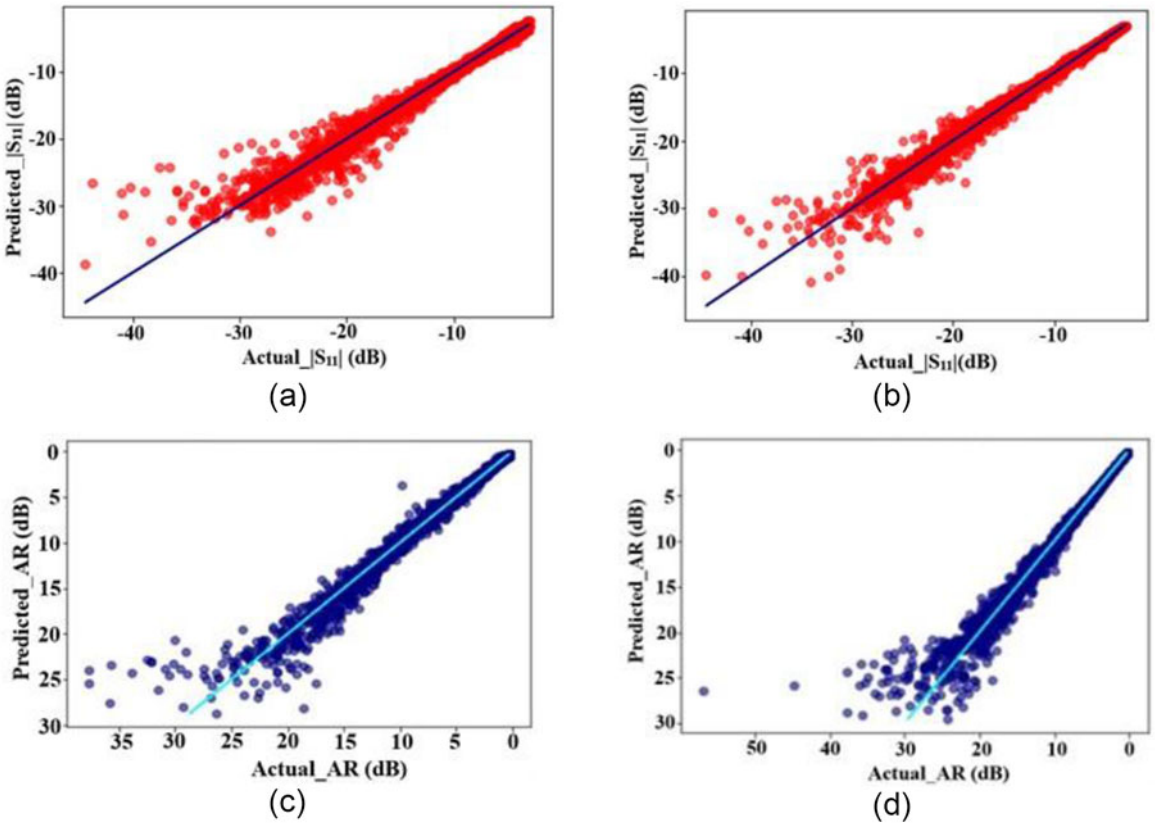


Figure 13. Comparison of the estimated and actual values: (a) decision tree_$|s_{11}|$, (b) random forest_$|s_{11}|$, (c) decision tree_axial ratio, and (d) random forest_axial ratio.

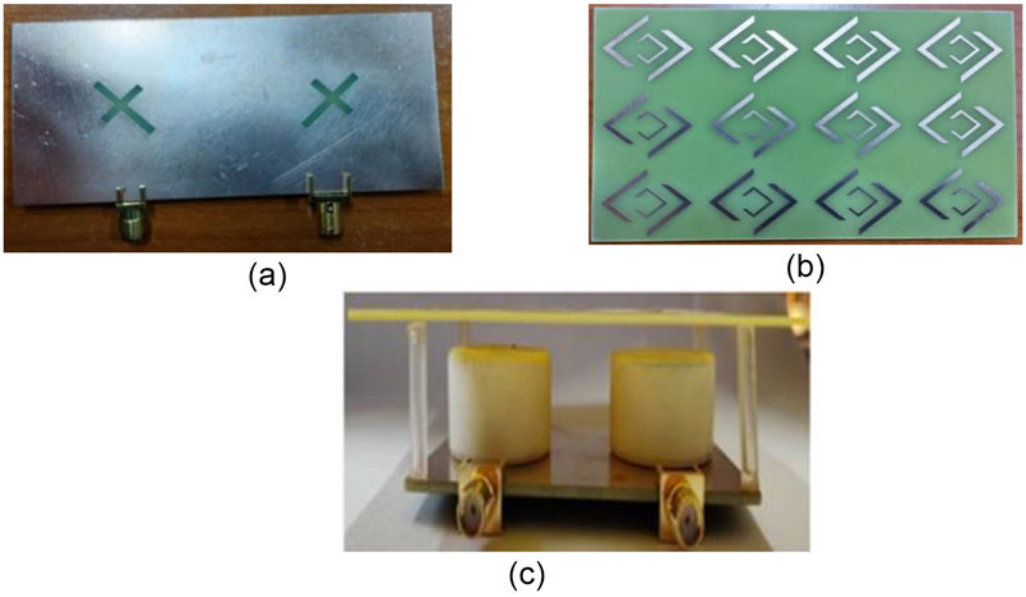


Figure 14. Fabricated prototype of designed aerial (a) feed layout (b) metasurface design (c) adjacent view.

step), L_F (27.0–32.0 mm in 0.25 incremental step), L_4 (3.0–7.0 mm in 0.25 incremental step), and L_3 (10.0–15.0 mm in 0.25 incremental step) with a frequency sweep from 7.0 GHz to 8.4 GHz with 51 points in between the mentioned range after the proposed antenna is designed with the assistance of HFSS. There were 25,041 dataset points in the entire created dataset. Thirty percent (7513) of the complete dataset are utilized for testing, while the remaining seventy percent (17,528) are used for training. A variety of loss parameters features, including as mean squared error (MSE), R-squared loss, and mean absolute error (MAE), are used to assess how well the planned antenna models perform [21]. Here, the four remaining antenna parameters – D, H, L_1, L_2, H_M, L_F, L_3, L_4, and

https://doi.org/10.1017/S1759078725101694 Published online by Cambridge University Press

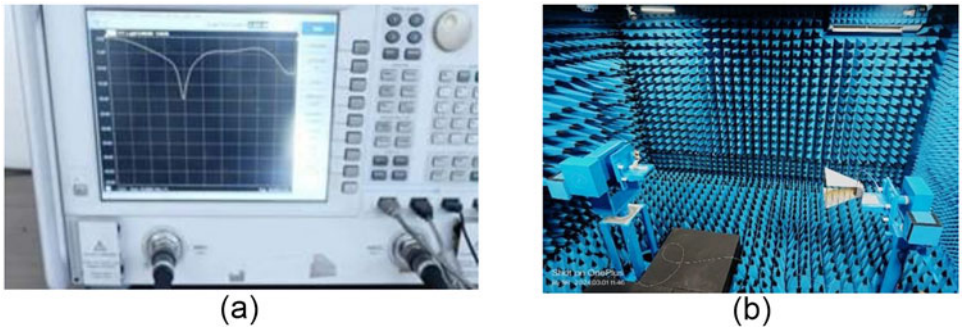


Figure 15. Pictures of measuring setup (a) VNA and (b) anechoic chamber.

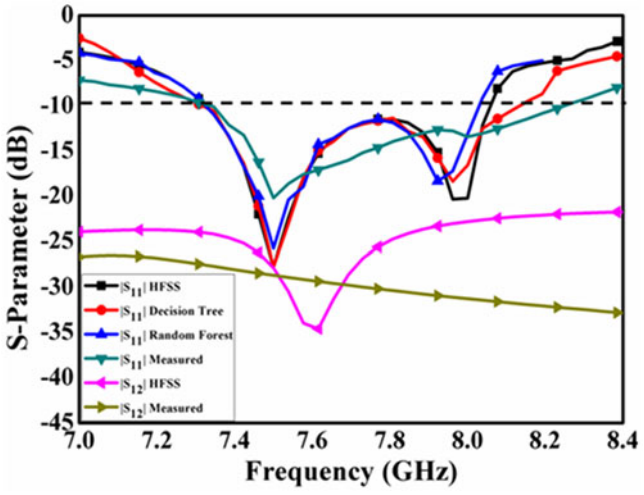


Figure 16. Measured/simulated/forecasted s-parameter of designed aerial.

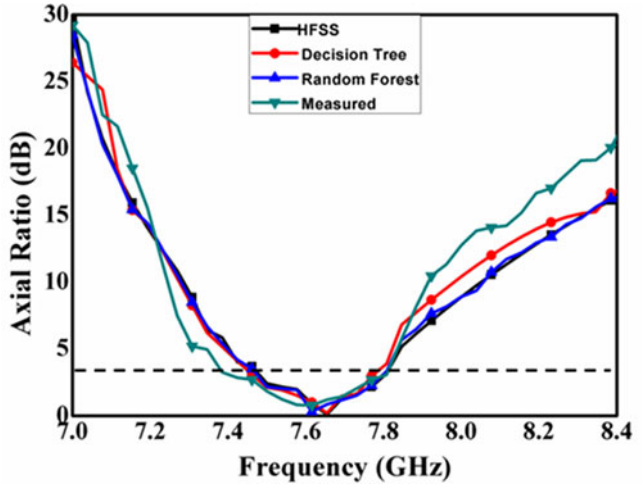


Figure 17. Measured/simulated/forecasted axial ratio alteration of designed aerial.

frequency – are regarded as input features, while S11 and axial ratio are taken as goal variables. Every ML method is trained, and then a validation dataset is used to evaluate every model. All of the outcomes produced by the various ML methods employed for S11 and axial ratio are compared in Tables 2 and 3, respectively. It can be shown from Tables 2 and 3 that random forest has the lowest mean error and the highest R^2 Score. Therefore, RF outperforms decision tree in performance prediction.

The anticipated vs. real outcomes graph for RF and Decision Tree on the test dataset for |S11| and axial ratio is shown in Fig. 13. The optimal scenario for regression issues is Y = X. Therefore, a higher density in the vicinity of the Y = X line indicates superior algorithmic performance. It can be shown from Fig. 13 that the random forest forecast is more accurate. For larger negative values of |S11|, the predicted value differed further from the real one.

Experimental verification

This section focuses on validating optimized simulated/forecasted machine learning outcomes with empirically acquired results. The designed aerial prototype is made and evaluated for this reason. In Fig. 14, it is displayed. Figure 15 shows the pictures of measuring set up i.e. vector network analyser (VNA) and anechoic chamber. Keysight's E5071C VNA is used to measure the S-parameter. The frequency range for Anechoic Chamber is from 1 to 18 GHz. The designed aerial's simulated, predicted, and measured S-parameter is shown in Fig. 16. There is good agreement among forecasted, simulated, and practically obtained S-parameter. The designed aerial works effectively in 7.21–8.2 GHz with the separation level more than 25 dB. Slight variance is obtained owing to the influence adhesive substance for adhering the ceramic over substrate. Addition of adhesive creates the small air gap between alumina ceramic and substrate. Due to this, there is reduction in impedance matching as well as shifting in the resonance peak [31].

Figure 17 presents the comparison of simulated/forecasted and experimentally attained axial ratio alteration for designed aerial. It is measured inside the anechoic chamber with the technique of dual linear far-field measurement [32]. It can be seen from Fig. 17 that there is good correlation among simulated, forecasted, and experimentally gained axial ratio. The designed aerial supports CP waves in between 7.35 and 7.8 GHz. Figure 18 shows the 2D measured/simulated LHCP and RHCP pattern at 7.6 GHz. Good corelation is obtained between experimental and simulated LHCP and RHCP pattern. In case of port-1, the LHCP is more dominant as compare to RHCP. That means, the port-1 supports LHCP waves from ceramic. Similarly, port-2 supports RHCP waves. Because of this, polarization diversity concept is supported by designed aerial. Broadsided far-field confirms the $HEM_{11\delta}$ mode inside the ceramic material. Figure 19 presents the experimental and simulated gain alteration of designed aerial. It is measured using two antenna technique [32]. Due to directive pattern, the maximum gain of designed aerial is approx. 11.5 dBi.

https://doi.org/10.1017/S1759078725101694 Published online by Cambridge University Press

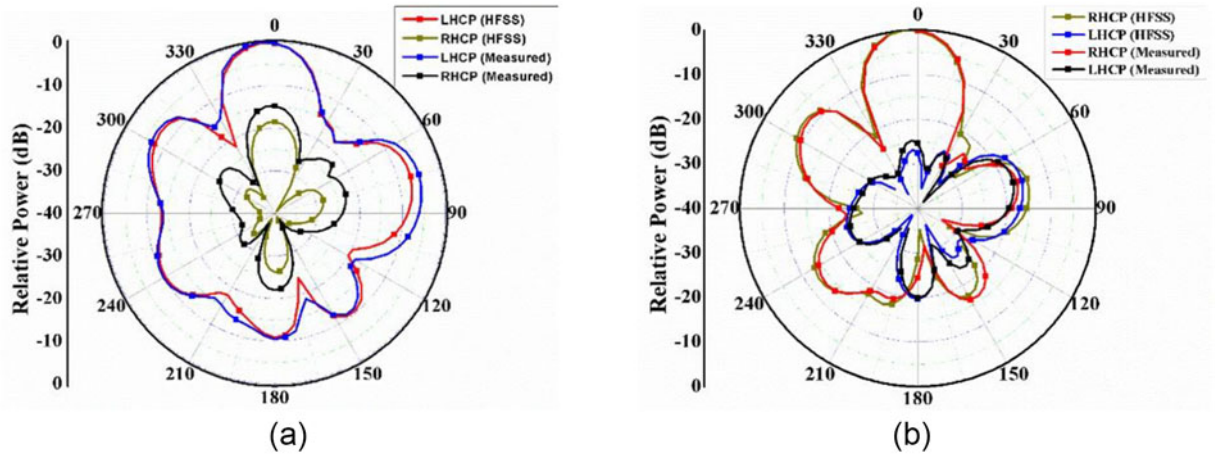


Figure 18. Measured/simulated LHCP and RHCP pattern at 7.6 ghz (a) port-1 (b) port-2.

Table 4. Comparing the designed twin band aerial's performance to published CP multiport ceramic aerials

Aerial structure	Working bandwidth (MHz)	AR bandwidth (MHz)	Gain (dBi)	No. of port	ML techniques	Isolation (dB)
Slot excited DR [5]	580	200	6.0	02	NA	>20
Printed Line stimulated DR [6]	2.4	320	3.0	02	NA	>15
X-formed slot excited RDR [7]	220	120	6.0	02	NA	>20
Slot Excited DR [8]	600	210	6.5	02	NA	>20
Slot Excited DR [9]	920	500	9.0	02	NA	>20
L-formed slot excited DR [14]	225	225	6.0	02	Yes	>15
Designed aerial	990	450	11.5	02	Yes	>25

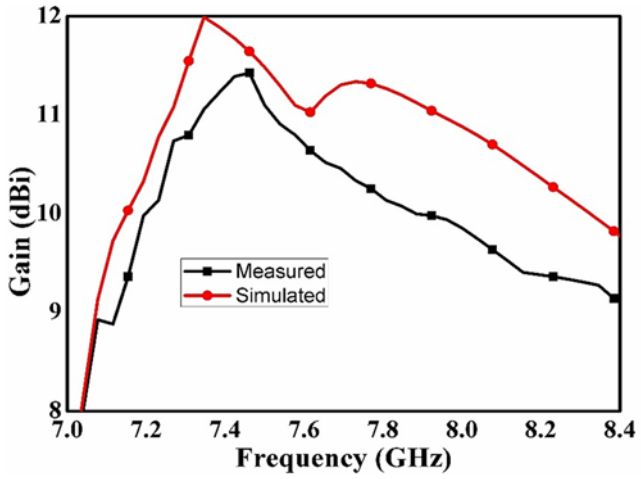


Figure 19. Measured/simulated gain alteration of designed aerial.

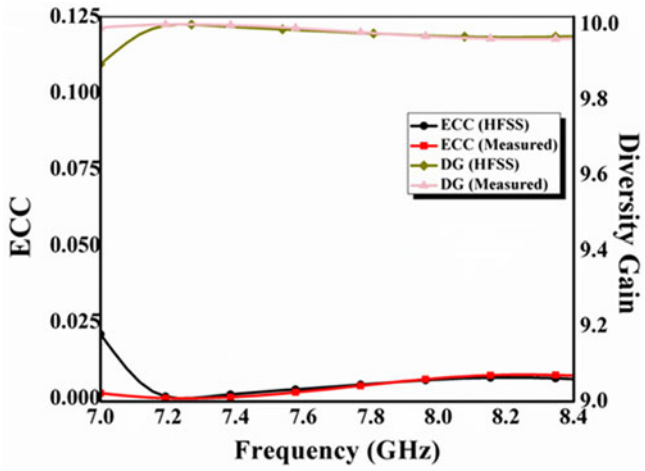


Figure 20. ECC and DG alteration of planned aerial.

Table 4 compares the performance of designed aerial with published two-port aerials on the basis of working range, aerial's gain and utilization of ML technique. The designed aerial provides wider impedance as well as axial ratio bandwidth. Aerial gain and isolation level between the ports of designed radiator is also quite high in comparison to published radiator. Last and important analysis for designed aerial is MIMO parameters, i.e. Envelop Correlation Coefficient (ECC) and diversity gain (DG). ECC talks about likeness among the antenna ports. It should be as low as (less than 0.2) possible for effective multi-port aerial. DG is directly related to ECC and talks about multi-port gain in fading

https://doi.org/10.1017/S1759078725101694 Published online by Cambridge University Press

situation [1]. There are well known formulas for calculating ECC and DG [1]. Figure 20 presents the simulated and experimental ECC and DG alteration for designed aerial. It can be seen from Fig. 20 that EEC is much lower than the standard, i.e. 0.2, while DG is approx. 10.0 within the working spectrum. This confirms the effectiveness of designed multi-port ceramic aerial.

Conclusion

A two-port ceramic-built aerial has been designed and examined in this communication. Some functioning factors such as, reflection coefficient and mutual coupling has also been predicted using Decision Tree and RF-based ML techniques. A metasurface made of double negative unit cells has been suspended over the twin port aerial for getting high gain, i.e. around 11.5 dBi. Cross slot with imbalanced arm size aids to produce circular waves in between 7.35 and 7.8 GHz. This antenna supports LHCP with port-1 and RHCP with port-2, which expands the separation level to 25 dB. With the help of fundamental hybrid modes, the designed aerial works in between 7.21 and 8.2 GHz. The major problem associated with the designed antenna is its bulky size due to the presence of MS. The aerial will work for deployment in 6G communication networks due to all these capabilities.

Funding statement. This research received no specific grant from any funding agency, commercial or not-for-profit sectors.

Competing interests. The authors report no conflict of interest.

References

1. **Sharawi MS** (2014) *Printed MIMO Antenna Engineering*. Boston, London: Artech House.
2. **Sharma A, Gupta S, Das G and Gangwar RK** (2020) Quad band quad sense circularly polarized dielectric resonator antenna for GPS/CNSS/WLAN/WiMAX applications. *IEEE Antennas and Wireless Propagation Letters* **19**, 403–408.
3. **Petosa A** (2007) *Dielectric Resonator Antenna Handbook*. Norwood, MA, USA: Artech House.
4. **Misilmani HE, Naous T and Khatib SA** (2020) A review on the design and optimization of antennas using machine learning algorithms and techniques. *International Journal of RF and Microwave Computer-Aided Engineering* **30**, 1–7.
5. **Das G, Sharma A and Gangwar RK** (2018) Dielectric resonator based circularly polarized MIMO antenna with polarization diversity. *Microwave and Optical Technology Letters* **60**, 685–690.
6. **Varshney G, Singh R, Pandey VS and Yaduvanshi RS** (2020) Circularly polarized two-port MIMO dielectric resonator antenna. *Progress In Electromagnetics Research M* **91**, 19–28.
7. **Hu Y, Pan YM and Yang MD** (2021) Circularly polarized MIMO dielectric resonator antenna with reduced mutual coupling. *IEEE Transactions on Antennas and Propagation* **69**, 3811–3819.
8. **Reddy GR, Prasad NR, Dwivedi AK, Singh V, Narayanaswamy NK and Sharma A** (2023) Metasurface–Loaded Ceramic–Based MIMO antenna with high isolation and circular polarization features. *Journal of Electronic Materials* **52**, 1305–1313.
9. **Yadav AK, Verma S, Penmatsa KKV and Sharma A** (2023) Linear to circular polarized wave convertor loaded dual port dielectric resonator antenna with enhanced gain for WLAN applications. *Electromagnetics* **43**, 407–417.
10. **Li J, Hu G, Shi L, He N, Li D, Shang Q, Zhang Q, Fu H, Zhou L, Xiong W, Guan J, Wang J, He S and Chen L** (2021) Full-color enhanced second harmonic generation using rainbow trapping in ultrathin hyperbolic metamaterials. *Nature Communications* **12**, 6425.
11. **Zhou E, Cheng Y, Chen F, Luo H and Li X** (2022) Low-profile high-gain wideband multi-resonance microstrip-fed slot antenna with anisotropic metasurface. *Progress In Electromagnetics Research* **175**, 91–104.
12. **Wang J, Cheng Y, Luo H, Chen F and Wu L** (2022) High-gain bidirectional radiative circularly polarized antenna based on focusing metasurface. *AEU - International Journal of Electronics and Communications* **151**, 154222.
13. **Zhang Z, Cheng Y, Luo H and Chen F** (2023) Low-profile wideband circular polarization metasurface antenna with characteristic mode analysis and mode suppression. *IEEE Antennas and Wireless Propagation Letters* **22**, 898–902.
14. **Huang Z, Zheng Y, Li J, Cheng Y, Wang J, Zhou ZK and Chen L** (2023) High-resolution metalens imaging polarimetry. *Nano Letters* **23**, 10991–10997.
15. **Deng M, Cotrufo M, Wang J, Dong J, Ruan Z, Alù A and Chen L** (2024) Broadband angular spectrum differentiation using dielectric metasurfaces. *Nature Communications* **15**, 2237.
16. **Feng S, Yang L, Cai B, Yang W, Wu L and Cheng Y** (2024) Tri-band terahertz metamaterial absorber based on structural $Ti_3C_2T_x$ MXene for enhanced sensing application. *IEEE Sensors Journal* **24**, 28889–28896.
17. **Yang W, Yang L, Cai B, Wu L, Feng S, Cheng Y, Chen F, Luo H and Li X** (2024) Efficiency tunable terahertz graphene metasurfaces for reflective single/dual-focusing effects based on Pancharatnam-Berry phase. *Results in Physics* **65**, 108003.
18. **Sun Y, Cai B, Yang L, Wu L, Cheng Y, Luo H, Chen F and Li X** (2024) High-gain dual-polarization microstrip antenna based on transmission focusing metasurface. *Materials* **17**, 3730.
19. **Zheng Z, Chen X and Huang K** (2010) Application of support vector machines to the antenna design. *International Journal of RF and Microwave Computer-Aided Engineering* **21**, 85–90.
20. **Sharma Y, Zhang HH and Xin H** (2020) Machine learning techniques for optimizing design of double T-shaped Monopole Antenna. *IEEE Transactions on Antennas and Propagation* **68**, 5658–5663.
21. **Ranjan P, Maurya A, Gupta H, Yadav S and Sharma A** (2022) Ultra-wideband CPW fed band-notched monopole antenna optimization using machine learning. *Progress in Electromagnetics Research M* **108**, 27–38.
22. **Srivastava A, Gupta H, Dwivedi AK, Penmatsa KKV, Ranjan P and Sharma A** (2022) Aperture coupled dielectric resonator antenna optimization using machine learning techniques. *AEU- International Journal of Electronics and Communications* **154**, 1–9.
23. **Pandey A, Singh AP and Kumar V** (2023) Design and optimization of circularly polarized dielectric resonator-based MIMO antenna using machine learning for 5G Sub-6 GHz. *AEU- International Journal of Electronics and Communications* **162**, 154558.
24. **Kajfez D, Glisson AW and James J** (1984) Computed modal field distributions for isolated dielectric resonators. *IEEE Transactions on Microwave Theory & Techniques* **32**, 1609–1616.
25. **Sharma A, Das G and Gangwar RK** (2018) Composite antenna for ultra-wide bandwidth applications: Exploring conceptual design strategies and analysis. *IEEE Antennas and Propagation Magazine* **60**, 57–65.
26. **Balanis CA** (2005) *Antenna Theory: Analysis and Design*. New York, USA: A John Wiley & Sons, INC., Publication.
27. **Numan AB and Sharawi MS** (2013) Extraction of material parameters for metamaterials using a full-wave simulator [education column]. *IEEE Antennas and Propagation Magazine* **55**, 202–211.
28. **Samantaray D and Bhattacharyya S** (2020) A gain-enhanced slotted patch antenna using metasurface as superstrate configuration. *IEEE Transactions on Antennas and Propagation* **68**, 6548–6556.
29. **Bhavani S, Raviteja B and Shanmuganantham T** (2025) Scarecrow-shaped antenna optimization using machine learning algorithms. *International Journal of Communication System* **38**, 1–9.
30. **Praveena A, Umamaheswari G, Rai JK, and Ranjan P** (2024) Machine learning enabled compact flexible full ground UWB antenna for wearable applications. *International Journal of Microwave and Wireless Technologies* **16**, 1–13.
31. **Faiz AM, Gogosh N, Khan SA and Shafique MF** (2014) Effects of an ordinary adhesive material on radiation characteristics of a dielectric resonator antenna. *Microwave and Optical Technology Letters* **56**, 1502–1506.

https://doi.org/10.1017/S1759078725101694 Published online by Cambridge University Press

32. **Stutzman GA and Thiele WL** (1998) *Antenna Theory and Design*. 2nd Hoboken, NJ, USA: Wiley.



Swati Anand Dwivedi received her B.E., M.E. Degree in Electronic and Communication from Rajiv Gandhi Technical University (Govt.), India. She is pursuing Ph.D. from Amity University Gwalior. She has more than 5 years of teaching and administrative experience.



Raghavendra Sharma completed his B. Tech. in Electrical Engineering from Dayalbagh Educational Institute (Deemed University) Agra, M.Tech in Electronic Design & Technology from Central Government Institute CEDTI Aurangabad (MS) and Ph.D. from Dayalbagh Educational Institute (Deemed University) Agra in the area of Signal Processing. In his teaching and research career of more than 25 years he has published more than 60 research papers in various Journals and Conferences of International & National repute (Scopus/SCI) and he is the editor of ETJRI (ISSN: 2581-8678) run by Amity University Madhya Pradesh Gwalior. He is Fellow of IETE and member of IEI, IETI (USA), IET, etc. He has filed more than 15 patents. He has guided more than 20 PG & PhD students, and his research interest lies in Digital Signal Processing, Image Processing, VLSI Design, Antenna Design, and Soft Computing.



Vivek Singh Kushwah (SMIEEE) received his B.E., M. Tech., and Ph.D. degree in Electronics & Communication Engineering from Rajiv Gandhi Technical University (Govt.), India. Presently, he is working as a Professor in Electronics and Communication Engineering Department at Chaitanya Bharathi Institute of Technology (A), Hyderabad, India. He has more than 17 years of teaching, research, and administrative experience. His research areas of interest include Artificial Neural Networks, Microstrip Antenna, R.F. and Microwave Filters, etc. He is associated with many SCI Journals and IEEE international conferences around the world as committee member, Reviewer and session chair. Presently, 4 Research Scholars are pursuing Ph.D. under his guidance and awarded 5 PhD Degrees, 92 B. Tech., and 1 M. Tech. Degree under his supervision. He evaluated 5 PhD Thesis. He received the *"International Researcher Award 2020-21"* and received *"Dainik Bhaskar Teachers Excellence Awards 2022"*.

https://doi.org/10.1017/S1759078725101694 Published online by Cambridge University Press